

Nematic Superconductivity and Its Critical Vestigial Phases in the Quasi-crystal

Yu-Bo Liu,^{1,*} Jing Zhou,^{2,3,*} and Fan Yang^{1,†}

¹*School of Physics, Beijing Institute of Technology, Beijing 100081, China*

²*Department of Science, Chongqing University of Posts and Telecommunications, Chongqing 400065, China*

³*Institute for Advanced Sciences, Chongqing University of Posts and Telecommunications, Chongqing, 400065, China*

We propose a general mechanism to realize nematic superconductivity (SC) and reveal its exotic vestigial phases in the quasi-crystal (QC). Starting from a Penrose Hubbard model, our microscopic studies suggest that the Kohn-Luttinger mechanism driven SC in the QC is usually gapless due to violation of Anderson's theorem, rendering that both chiral and nematic SCs are common. The nematic SC in the QC can support novel vestigial phases driven by pairing phase fluctuations above its T_c . Our combined renormalization group and Monte-Carlo studies provide a phase diagram in which, besides the conventional charge-4e SC, two critical vestigial phases emerge, i.e. the quasi-nematic (Q-N) SC and Q-N metal. In the two Q-N phases, the discrete lattice rotation symmetry is counter-intuitively "quasi-broken" with power-law decaying orientation correlations. They separate the phase diagram into various phases connected via Brezinskii-Kosterlitz-Thouless (BKT) transitions. These remarkable critical vestigial phases, which resemble the intermediate BKT phase in the q -state ($q \geq 5$) clock model, are consequence of the five- (or higher-) fold anisotropy field brought about by the unique QC symmetry, which are absent in conventional crystalline materials.

Introduction: The electron states in the quasicrystal (QC) are attracting more and more attentions recently [1–17]. Due to its special long-range order without translation period, the QC can host such as five- or eight-fold rotation symmetry forbidden in crystals. Various correlated [18–29] and topological [30–44] electron states have been revealed in the QC. Particularly, the discovery of superconductivity (SC) in the Al-Zn-Mg QC [45] has aroused many interests recently [46–59]. Theoretically, the pairing symmetries in such QC as the 2D Penrose lattice have been classified [3] according to the irreducible representation (IRRP) of the D_5 point group. Remarkably, the 2D IRRPs can lead to chiral SC hosting spontaneous bulk current, driven by repulsive interaction via the Kohn-Luttinger (K-L) mechanism. Here we propose that gapless nematic SC can also be a common pairing phase in QCs. More interesting, partial melting of this order can lead to two critical vestigial phases, i.e. the quasi-nematic (Q-N) SC and Q-N metal, which are protected by the unique QC symmetry absent in crystals.

Generally in a pairing state belonging to the 2D IRRP of the point group, the two basis gap functions can be $1 : i$ or $1 : r$ ($r \in R$) mixed. In crystals, the $1 : i$ mixing is usually energetically favored as it generates a full pairing gap [61]. However, the situation is distinct in QCs: It has been shown that, the Anderson's theorem [62], which states that an electron state tends to pair with its time-reversal partner, is violated in a K-L mechanism driven pairing phase in a QC [3]. Here we show that the violation of this theorem usually leads to gapless SC, which renders that both the chiral and nematic SCs are common in QCs, and we further focus on the finite-temperature vestigial phases [63–78] of the nematic SC.

The nematic SC [79–84] spontaneously breaks the $U(1)$ -gauge and lattice rotation symmetries. For the continuous $U(1)$ -gauge symmetry, there exists a Brezinskii-

Kosterlitz-Thouless (BKT) transition temperature T_{BKT} below which the pairing correlation power-law decays. For the discrete lattice-rotation symmetry, there usually exists a second-order transition temperature T_{nem} below which long-range nematic order develops. When $T_{\text{BKT}} \neq T_{\text{nem}}$, two vestigial phases can emerge above T_c of the nematic SC, i.e. the charge-4e SC or the nematic metal [77, 78]. Here we demonstrate that for the nematic SC on the Penrose lattice, there exists an intermediate-temperature regime, wherein the discrete lattice-rotation symmetry is counter-intuitively "quasi-broken", leading to extended critical vestigial phases with power-law decaying orientation correlations, dubbed as Q-N phases.

In this paper, we start from a Penrose Hubbard model. Based on the K-L mechanism, our microscopic calculations suggest that the violation of Anderson's theorem usually leads to gapless SC with finite zero-energy density of state (DOS). For the 2D IRRPs of D_5 , our combined Ginzburg-Landau (G-L) analysis and microscopic energy calculations can lead to either chiral or nematic SCs for different parameters. We then study the vestigial phases of the nematic SC driven by the phase fluctuations of the two pairing components, via combined renormalization group (RG) and Monte-Carlo (MC) approaches. In the obtained phase diagram, besides the charge-4e SC, two critical vestigial phases emerge, i.e. the Q-N SC and Q-N metal (MT), which render that all phase transitions are BKT like. The two remarkable critical phases, which resemble the intermediate BKT phase of the q -state ($q \geq 5$) clock model, are brought about by the five- (or higher-) fold anisotropy field caused by the unique QC symmetry, which are absent in crystals.

Model and Gapless Nematic SC: Let us consider the following Hubbard model on the Penrose lattice,

$$H = - \sum_{\langle i,j \rangle \sigma} t c_{i\sigma}^\dagger c_{j\sigma} + U \sum_i n_{i\uparrow} n_{i\downarrow} - \mu \sum_{i,\sigma} n_{i\sigma}, \quad (1)$$

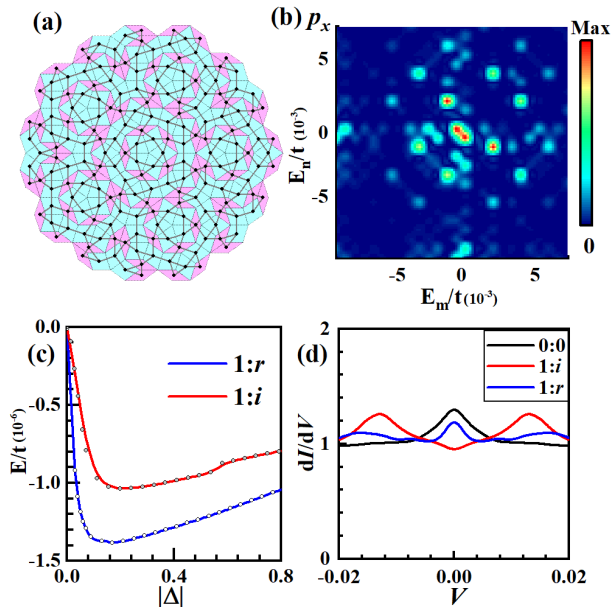


FIG. 1. (Color online) (a) Schematic diagram of Penrose lattice. The lattice sites at the center of the rhombuses are marked by solid black circles. NN bonding is marked by solid gray lines. (b) Contour plots of relative $|\Delta_{mn}|$, for a singlet p_x -wave pairing for $\delta = 0.49$ and $U/W_D = 0.5$. (c) Ground state energy E as function of the global magnitude $|\Delta|$ for the pairing with $1:r$ (blue, minimized for r) and $1:i$ (red) mixing of the two degenerate basis functions. The energy E is in unit of t in (b-c). (d) STM dI/dV of a typical site for the nematic SC (blue), chiral SC (red) and normal state (black).

where $c_{i\sigma}$ annihilates an electron at site i with spin σ , $n_{i\sigma}$ is the electron-number operator, and μ denotes the chemical potential. Here the lattice sites are defined as the centers of the rhombuses on the Penrose tiling, as marked by the black solid circles in Fig. 1(a). We define two rhombuses sharing an edge as nearest neighbor (NN) [85, 86], and only consider hoppings along the NN bonds, as marked by the solid lines in Fig. 1(a). The tight-binding part of Eq. (A1) is diagonalized as $H_{TB} = \sum_{m\sigma} \tilde{\epsilon}_m c_{m\sigma}^\dagger c_{m\sigma}$, with $c_{m\sigma} = \sum_i \xi_{i,m} c_{i\sigma}$. Here m labels a single-particle eigen state with eigen-energy $\tilde{\epsilon}_m = \epsilon_m - \mu$ and eigenstate $\xi_{i,m}$. The total band width is $W_D \approx 8t$. We adopt $U = 0.5W_D$ in our calculations.

The Cooper pairing in this system can be driven by the K-L mechanism [87, 88], generalized to the cases in the QC [3]. In this mechanism, two electrons near the Fermi level can gain effective attraction through exchanging particle-hole excitations in several second-order perturbative processes. Then a BCS mean-field (MF) treatment on the obtained effective Hamiltonian provides the self-consistent gap equation, which after linearized near T_c takes the form of an eigenvalue problem of the interaction matrix. The T_c is given by the temperature at which the largest eigenvalue of this matrix attains one, and the

pairing symmetry, classified according to the IRRPs of D_5 , is determined by the corresponding eigenvector. See the Supplementary Materials (SM) [89] for details.

In Fig. 1(b), we show distribution of the amplitude $|\Delta_{mn}|$ ($\Delta_{mn} \in R$) of a typical singlet p_x -wave pairing gap function between the states m and n (labeled by their energies) near the Fermi level, obtained at the filling $\delta = 0.49$. That of the p_y -symmetry in the same 2D (p_x, p_y) IRRP is given in the SM [89]. Fig. 1(b) displays that for each m , there is no unique n rendering $|\Delta_{mn}|$ dominates that of any other n , violating Anderson's theorem. The BCS-MF Hamiltonian for this pairing state reads

$$H_{\text{BCS-MF}} = \sum_{m\sigma} \tilde{\epsilon}_m c_{m\sigma}^\dagger c_{m\sigma} + \sum_{m,n} \left(c_{m\uparrow}^\dagger c_{n\downarrow}^\dagger - c_{m\downarrow}^\dagger c_{n\uparrow}^\dagger \right) \Delta_{mn} + h.c. \quad (2)$$

If $\Delta_{mn} = \Delta_m \delta_{mn}$, Eq. (2) is diagonalized to yield the Bogoliubov quasi-particle dispersion $E_m = \sqrt{\tilde{\epsilon}_m^2 + \Delta_m^2}$, under which the condition $E_m = 0$ leads to two combined equations: $\tilde{\epsilon}_m = 0; \Delta_m = 0$. In 2D at thermal-dynamic limit, the two equations lead to at most isolate solutions for m , corresponding to point gap nodes or full gap. However, due to violation of Anderson's theorem here, E_m no longer takes this simple analytical form. Consequently, $E_m = 0$ only provides one equation, which in 2D usually leads to an $O(L)$ (L : lattice size) number of m , forming a gapless SC carrying finite zero-energy DOS.

The mixing ratio between the two basis gap functions of a 2D IRRP, e.g. $(\Delta_{p_x}, \Delta_{p_y})$, is analyzed via the G-L theory given in the SM [89]. For convenience, we rotate the bases as $\Delta_\pm = \Delta_{p_x} \pm i\Delta_{p_y}$. The transformation of Δ_\pm under the C_5^1 rotation is $\hat{P}_{2\pi/5} \Delta_\pm(\mathbf{r}) = e^{\pm 2i\pi/5} \Delta_\pm(\mathbf{r})$. Under the mirror reflection, Δ_\pm mutually exchange. The mixed gap function is $\Delta = \psi_+ \Delta_+ + \psi_- \Delta_-$. Fixing Δ_\pm , the G-L free energy $F = F(\psi_+, \psi_-)$ can only take the following $D_5 \otimes U(1)$ -gauge symmetry-allowed form [89]

$$F(\psi_+, \psi_-) = \alpha(|\psi_+|^2 + |\psi_-|^2) + \beta(|\psi_+|^4 + |\psi_-|^4) + \gamma|\psi_+|^2|\psi_-|^2 + O(\psi_\pm^6) \quad (3)$$

If $\gamma > 2\beta$, F is minimized at $\psi_+ = 0$ or $\psi_- = 0$, leading to a chiral SC wherein Δ_{p_x} and Δ_{p_y} are $1:i$ mixed; if $\gamma < 2\beta$, F is minimized at $|\psi_+|/|\psi_-| = 1$, leading to a nematic SC wherein Δ_{p_x} and Δ_{p_y} are $1:r$ mixed ($r \in R$).

To determine the realized ground state, we calculate the energy E as function of the global amplitude Δ for the $1:r$ (minimized for r) and $1:i$ mixing cases. As shown in Fig. 1(c), the energy of the $1:r$ mixing is lower, suggesting a nematic SC ground state. This result seems conflicting with the intuition that the chiral SC is usually energetically favored due to opening of a full pairing gap [61]. This counter-intuitive result can be explained by Fig. 1(d) which displays the local DOS detected by the STM dI/dV curve for a typical site (that for more sites

are given in the SM [89]). Fig. 1(d) shows that both the chiral and nematic SCs are gapless. Therefore in QCs, the chiral SC loses its advantage in energy, rendering that the nematic SC is also common. Note that chiral SC is also possible in this system, see the case at $\delta = 0.51$ [89]. The gapless SC resembles the standard Fermi liquid in nature of elementary excitations, reflected in such quantities as the linearly temperature-dependent specific heat and saturate Knight-shift when $T \rightarrow 0$. However, this state carries nonzero superfluid density. See the SM [89].

Phase Diagram and Vestigial Phases: Above the T_c of nematic SC, nontrivial vestigial phases can be driven by the phase fluctuations of its two pairing components [77, 78]. Under thermal fluctuations, the global amplitudes ψ_{\pm} appearing in Eq. (3) become functions of the coarse-grained position \mathbf{r} . Despite lack of translation period, the QC is uniform in the long-wave limit [40, 90]. Therefore, $\psi_{\pm}(\mathbf{r})$ is smooth function of \mathbf{r} . Focusing on low-energy phase fluctuations, we set $\psi_{\pm}(\mathbf{r}) = \psi_0 e^{i\theta_{\pm}(\mathbf{r})}$, with the constant $\psi_0 > 0$ and pairing phases $\theta_{\pm}(\mathbf{r}) \in (0, 2\pi)$. To include dependence on $\theta_{\pm}(\mathbf{r})$, the free energy functional F is expanded to $O(\psi_{\pm}^{10})$ as [89]

$$F^{(10)}(\psi_+, \psi_-) = -A_0 (\psi_+^5 \psi_-^{5*} + \text{c.c.}) + O(\psi^{12}). \quad (4)$$

Let's introduce the global and relative phase fields θ and ϕ through $\theta_{\pm}(\mathbf{r}) = \theta(\mathbf{r}) \pm \phi(\mathbf{r})$. Physically, ordering of the θ field breaks the U(1)-gauge symmetry and represents for SC, while ordering of the ϕ field breaks the rotation symmetry and indicates the nematic order. When dependence on $\nabla\theta$ and $\nabla\phi$ is included [77], the low-energy classical Hamiltonian is given as,

$$H = \int d^2\mathbf{r} \left(\frac{\rho}{2} |\nabla\theta|^2 + \frac{\kappa}{2} |\nabla\phi|^2 - A \cos 10\phi \right). \quad (5)$$

Here ρ/κ are stiffness parameters, and $A = 2A_0\psi_0^{10}$.

Eq. (5) shows that, while the Hamiltonian for the θ field describes a continuous-space pure XY model, that for the ϕ field describes a continuous-space XY model subject to a q -fold ($q = 5$) anisotropy field, resembling the q -state clock model in symmetry. Note that $(\theta(\mathbf{r}), \phi(\mathbf{r}) + \pi)$ and $(\theta(\mathbf{r}), \phi(\mathbf{r}))$ describe gauge equivalent states as their corresponding physical $(\theta_+(\mathbf{r}), \theta_-(\mathbf{r}))$ configurations are only globally different by a constant π [4]. Therefore, the seeming ten saddle points for the ϕ field in Eq. (5) actually represent for five ones, causing the five-fold anisotropy. In (5), the θ and ϕ fields are subject to the constraint that both fields should host integer or half-integer vortices simultaneously [63–66].

We employ the RG approach to study the model (5), and map it to a dual two-component Sine-Gordon model described by the following action [77],

$$S_{\text{SG}} = \int d^2\mathbf{x} \left(\frac{T}{2\rho} |\nabla\tilde{\theta}|^2 + \frac{T}{2\kappa} |\nabla\tilde{\phi}|^2 - g_{10} \cos 10\phi - g_{2,0} \times \cos 2\pi\tilde{\theta} - g_{0,2} \cos 2\pi\tilde{\phi} - g_{1,1} \cos \pi\tilde{\theta} \cos \pi\tilde{\phi} \right), \quad (6)$$

TABLE I. Correspondence between RG fixed points and phases. The new abbreviations denote: MT (normal metal), 4e-SC(charge-4e SC), N-SC (nematic SC).

$g_{2,0}$	∞	0	∞	0	0
$g_{0,2}$	∞	∞	0	0	0
$g_{1,1}$	∞	0	0	0	0
g_{10}	0	0	0	0	∞
phase	MT	4e-SC	Q-N MT	Q-N SC	N-SC

where $\tilde{\theta}/\tilde{\phi}$ are dual vortex fields of θ/ϕ . Here $g_{2,0}/g_{0,2}$ are fugacities for integer $\tilde{\theta}/\tilde{\phi}$ vortices while $g_{1,1}$ is the fugacity for half ϕ -half θ vortices, and $g_{10} \propto A$ is the anisotropy parameter. While details of the RG approach including the one-loop RG flow equation are provided in the SM [89], the correspondence between the available fixed points and the phases are illustrated in Tab. II.

The RG phase diagram is shown in Fig. 2(a), which is topologically insensitive to the initial values of the coupling parameters [89]. When $T \rightarrow 0$, all fugacities are irrelevant while g_{10} is relevant, forming the nematic SC (N-SC). When T arises, the system first enters the Q-N SC when g_{10} becomes irrelevant. When T further enhances, if $\kappa < \rho$, the Q-N SC turns into the charge-4e SC (4e-SC) once $g_{0,2}$ gets relevant rendering proliferation of the ϕ vortices; if $\kappa > \rho$, the Q-N SC turns into the Q-N MT once $g_{2,0}$ gets relevant rendering proliferation of the θ vortices. When T is high enough, the normal MT is achieved for whatever κ/ρ . If $\kappa \approx \rho$, when T arises, the Q-N SC directly turns into the MT once $g_{1,1}$ gets relevant rendering proliferation of the half ϕ -half θ vortices.

Quasi-Nematic Phases: Two new phases absent in previous studies [77, 78] emerge in the phase diagram Fig. 2(a) and Tab. II: the Q-N SC and Q-N MT. These two Q-N phases are realized when the fugacity $g_{0,2}$ is irrelevant so that no free ϕ -vortex is excited, but the 5-fold anisotropy parameter g_{10} for the ϕ -field is irrelevant. To further study the nature of the two new phases and their phase transitions, we perform a MC study [89] on a discretized version of the continuous Hamiltonian (5). The obtained specific heat, superfluid density, susceptibilities, Binder cumulants and correlation functions [89] combinedly provide the phase diagram shown in Fig. 2(b), which is topologically consistent with Fig. 2(a).

Taking three typical $\kappa/\rho = 0.3, 1, 2.2$ marked in Fig. 2(b), we display the temperature T/ρ dependence of the specific heat C_v and the ϕ -field susceptibility χ_{ϕ} on different lattice sizes ($L = 40, 60, 80$) in Fig. 2(c-e) and (f-h), respectively. The grey dashed lines in (c-h) mark the phase transitions. For C_v (c-e), the phase transitions either showcase as broad humps or are featureless, which are insensitive to L , implying that no singularity will emerge upon $L \rightarrow \infty$, suggesting that all the transi-

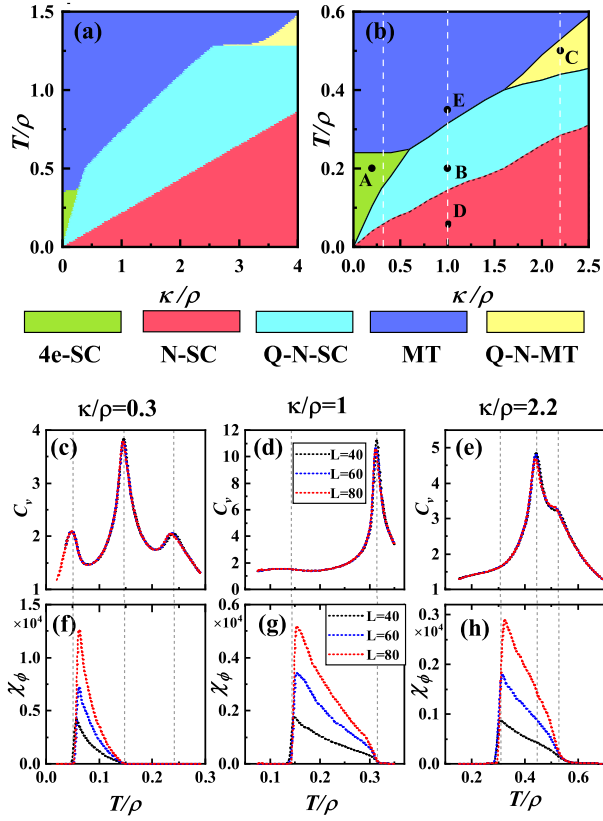


FIG. 2. (Color online) Phase diagrams provided by (a) the RG- and (b) the MC- studies. The initial values of the coupling parameters for obtaining (a) are $g_{2,0} = g_{0,2} = 0.1$, $g_{1,1} = 0.01$, $g_{10} = 0.001$ and for (b) are $A = 0.025\rho$. The white dashed lines in (b) represent $\kappa/\rho = 0.3, 1, 2.2$, respectively. (c-e) Specific heat C_v and (f-h) the ϕ -field susceptibility χ_ϕ as function of temperature T/ρ on different lattice sizes ($L = 40, 60, 80$) for $\kappa/\rho = 0.3$ in (c) and (f), $\kappa/\rho = 1$ in (d) and (g), and $\kappa/\rho = 2.2$ in (e) and (h). The grey dashed lines in (c)-(h) mark the phase transitions.

tions are BKT-like. While it's known that the superconducting transition in 2D is BKT-like, here it's remarkable that the phase transitions related to the breaking of the discrete lattice-rotation symmetry are also BKT-like. This point is related to the T/ρ dependence of χ_ϕ (f-h): While it is finite and small in the low- T nematic phase (N-SC) and high- T non-nematic phases (4e-SC and MT), it strongly depends on L and diverges upon $L \rightarrow \infty$ in the intermediate- T Q-N phases (Q-N SC and Q-N MT) resembling the divergence of χ_θ in the superconducting phases [89], suggesting that the Q-N phases are BKT-like extended critical phases for the ϕ -field. The transitions from the Q-N phases to the nematic or non-nematic phases are BKT-like.

The nature of the two Q-N phases is reflected in the correlation functions $\eta_\theta(\Delta\mathbf{r}) \equiv \frac{1}{N} \sum_{\mathbf{r}} \langle e^{i[\theta(\mathbf{r}) - \theta(\mathbf{r} + \Delta\mathbf{r})]} \rangle$ and η_ϕ defined similarly. Fig. 3(a) and (b) show Δr ($\equiv |\Delta\mathbf{r}|$)-dependence of η_ϕ and η_θ for the typical point B

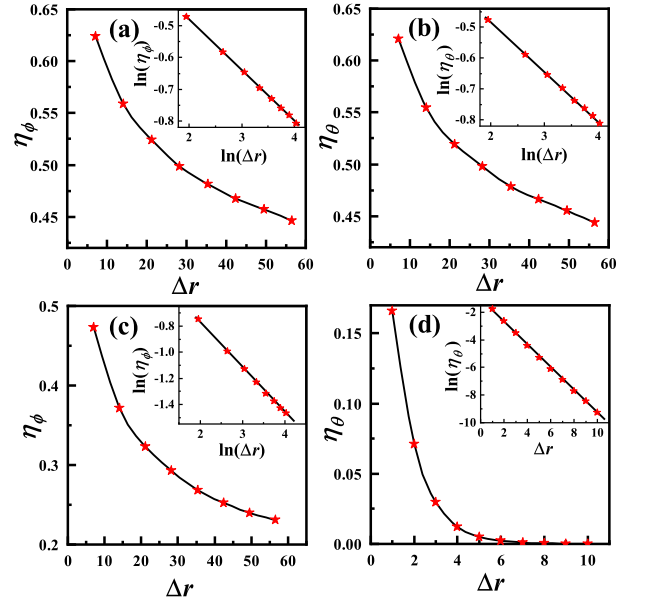


FIG. 3. (Color online) The correlation function $\eta_{\phi/\theta}$ for (a) and (b) for the point B ($\kappa = 0.1\rho, T = 0.2\rho$), for (c) and (d) for the point C ($\kappa = 2.2\rho, T = 0.5\rho$) marked in Fig. 2(b). Insets of (a-c) the log-log plot, and (d) only the y-axis is logarithmic. The $\eta_{\phi/\theta}$ for A, D, E are given in the SM [89].

marked in Fig. 2(b). Obviously, both η_θ and η_ϕ power-law decay with Δr , reflecting the Q-N SC. Fig. 3(c) and (d) are for the typical point C marked in Fig. 2(b): While η_θ decays exponentially with Δr , η_ϕ power-law decays with Δr , reflecting the Q-N MT. The common feature for the two Q-N phases is power-law decaying of $\eta_\phi \sim \Delta r$, indicating the quasi-long-range order of the ϕ field, suggesting that the discrete lattice-rotation symmetry has been remarkably “quasi-broken”.

Discussion and Conclusion: The counterintuitive Q-N phases obtained here bear resemblance to the intermediate BKT phase in the 2D q -state clock model for $q \geq 5$ [92–98], which also exhibits power-law decaying correlation and BKT transitions to adjacent phases. Such intriguing phase fluctuation driven Q-N phases can only emerge on QCs: As derived in the SM [89], for a D_{2n} (D_{2n+1}) symmetric lattice, the anisotropy-field Hamiltonian for the ϕ field is $-A \cos(2n\phi)$ ($-A \cos[2(2n+1)\phi]$), leading to the $n(2n+1)$ fold anisotropy, resembling the $n(2n+1)$ -state clock model in symmetry. Consequently, only the D_5, D_7 or $D_n (n \geq 9)$ lattices can host the Q-N phases, which can only be realized on QCs.

In conclusion, the SC driven by K-L mechanism in the QC violates Anderson's theorem, allowing the ground state to be either chiral or nematic SC. We have further investigated the vestigial phases of this nematic SC by combined RG and MC methods. Our results suggest the emergence of the remarkable Q-N SC and Q-N MT phases, supported by the unique QC symmetry.

Note: Shortly after this work was finished and announced, another highly related work also emerged [99], in which the “critical nematic phase” (which has the same physical meaning as the “quasi-nematic phase” dubbed here) is revealed as possible vestigial phase of the nematic superconductivity on the 30°-twisted hexagonal bilayer, which hosts 12 fold quasi-crystal rotation symmetry.

Acknowledgements: This work is supported by the NSFC under the Grant Nos. 12074031, 12234016 and the funding of Institute for Advanced Sciences of Chongqing University of Posts and Telecommunications (E011A2022326).

* These two authors contributed equally to this work.

† yangfan_blg@bit.edu.cn

- [1] M. A. Bandres, M. C. Rechtsman, and M. Segev, Topological Photonic Quasicrystals: Fractal Topological Spectrum and Protected Transport, *Phys. Rev. X* **6**, 011016 (2016).
- [2] K. Giergiel, A. Kuroki, and K. Sacha, Discrete time quasicrystals, *Phys. Rev. B* **99**, 220303(R) (2019).
- [3] E. D. Roberts, R. M. Fernandes, and A. Kamenev, Nature of protected zero-energy states in Penrose quasicrystals *Phys. Rev. B* **102** 064210 (2020).
- [4] S. Sakai and A. Koga, Effect of Electron-Electron Interactions on Metallic State in Quasicrystals. *Mater. Trans.* **62** 380 (2021).
- [5] J. B. Hauck, C. Honerkamp, S. Achilles, and D. M. Kennes, Electronic instabilities in Penrose quasicrystals: Competition, coexistence, and collaboration of order. *Phys. Rev. Research* **3** 023180 (2021).
- [6] S. Sakai and N. Takemori, Doped Mott insulator on a Penrose tiling. *Phys. Rev. B* **105** 205138 (2022)
- [7] K. Inayoshi, Y. Murakami, and A. Koga, Photoinduced dynamics of a quasicrystalline excitonic insulator. *Phys. Rev. B* **105** 104307 (2022)
- [8] S. Sakai, R. Arita, and T. Ohtsuki, Hyperuniform electron distributions controlled by electron interactions in quasicrystals. *Phys. Rev. B* **105** 054202 (2022)
- [9] S. Sakai, R. Arita, and T. Ohtsuki, Quantum phase transition between hyperuniform density distributions. *Phys. Rev. Research* **4** 033241 (2022).
- [10] O. Lesser and R. Lifshitz, Emergence of quasiperiodic Bloch wave functions in quasicrystals. *Phys. Rev. Research* **4** 013226 (2022).
- [11] M. A. Keskiner and M. O. Oktel, Strictly, localized states on the Socolar dodecagonal lattice. *Phys. Rev. B* **106** 064207 (2022).
- [12] Y. Nagai, Intrinsic vortex pinning in superconducting quasicrystals. *Phys. Rev. B* **106** 064506 (2022).
- [13] S. Sakai, Hyperuniform electron distributions on the Ammann-Beenker tiling. *J. Phys.: Conf. Ser.* **2461** 012002 (2023)
- [14] A. Jagannathan and M. Tarzia, Electronic states of a disordered two-dimensional quasiperiodic tiling: From critical states to Anderson localization. *Phys. Rev. B* **107** 054206 (2023).
- [15] A. Jagannathan, Closing of gaps, gap labeling, and passage from molecular states to critical states in a two-dimensional quasicrystal. *Phys. Rev. B* **108** 115109 (2023).
- [16] M. Ciardi, A. Angelone, F. Mezzacapo, and F. Cinti, Quasicrystalline Bose Glass in the Absence of Disorder and Quasidisorder. *Phys. Rev. Lett.* **131**, 173402 (2023).
- [17] M. A. Keskiner, O. Erten, and M. O. Oktel, Kitaev-type spin liquid on a quasicrystal. *Phys. Rev. B* **108** (2023).
- [18] S. Wessel, A. Jagannathan, and S. Haas, Quantum Antiferromagnetism in Quasicrystals, *Phys. Rev. Lett.* **90**, 177205 (2003).
- [19] V. R. Shaginyan, A. Z. Msezane, K. G. Popov, G. S. Japaridze, and V. A. Khodel, Common quantum phase transition in quasicrystals and heavy-fermion metals, *Phys. Rev. B* **87**, 245122 (2013).
- [20] S. Thiem and J. T. Chalker, Long-range magnetic order in models for rare-earth quasicrystals, *Phys. Rev. B* **92**, 224409(2015).
- [21] E. C. Andrade, A. Jagannathan, E. Miranda, M. Vojta, and V. Dobrosavljevic, Non-Fermi-Liquid Behavior in Metallic Quasicrystals with Local Magnetic Moments, *Phys. Rev. Lett.* **115**, 036403 (2015).
- [22] J. Otsuki and H. Kusunose, Distributed hybridization model for quantum critical behavior in magnetic quasicrystals, *J. Phys. Soc. Jpn.* **85**, 073712 (2016).
- [23] A. Koga and H. Tsunetsugu, Antiferromagnetic order in the Hubbard model on the Penrose lattice, *Phys. Rev. B* **96**, 214402 (2017).
- [24] H. Miyazaki, T. Sugimoto, K. Morita, and T. Tohyama, Magnetic orders induced by RKKY interaction in Tsai-type quasicrystalline approximant Au-Al-Gd *Phys. Rev. Materials* **4** 024417 (2020).
- [25] A. Koga, Antiferromagnetically Ordered State in the Half-Filled Hubbard Model on the Socolar Dodecagonal Tiling. *Mater. Trans.* **textbf62** 360 (2021).
- [26] A. Koga and S. Coates, Ferrimagnetically ordered states in the Hubbard model on the hexagonal golden-mean tiling. *Phys. Rev. B* **105** 104410 (2022).
- [27] P. Ghosh, Exact quantum ground state of a two-dimensional quasicrystalline antiferromagnet. *Phys. Rev. B* **108**, 014426 (2023).
- [28] T. Sugimoto, S. Suzuki, R. Tamura, T. Tohyama, Revisit of magnetic orders in 1/1 approximant crystals of Tsai-type quasicrystal from theoretical points of view. *arXiv:2311.08055* (2023).
- [29] R. N. Araujo, C. C. Bellinati, E. C. Andrade, Fragile magnetic order in metallic quasicrystals. *arXiv:2312.10192* (2023).
- [30] Y. E. Kraus, Y. Lahini, Z. Ringel, M. Verbin, and O. Zeitlinger, Topological States and Adiabatic Pumping in Quasicrystals, *Phys. Rev. Lett.* **109**, 106402 (2012).
- [31] H. Huang and F. Liu, Quantum Spin Hall Effect and Spin Bott Index in a Quasicrystal Lattice, *Phys. Rev. Lett.* **121**, 126401 (2018).
- [32] H. Huang and F. Liu, Comparison of quantum spin Hall states in quasicrystals and crystals, *Phys. Rev. B* **100**, 085119 (2019).
- [33] S. Longhi, Topological Phase Transition in non-Hermitian Quasicrystals, *Phys. Rev. Lett.* **122**, 237601 (2019).
- [34] S. Spurrier and N. R. Cooper, Kane-Mele with a twist: Quasicrystalline higher-order topological insulators with fractional mass kinks. *Phys. Rev. Research* **2**, 033071 (2020).

- [35] R. Ghadimi, T. Sugimoto, K. Tanaka, and T. Tohyama, Topological superconductivity in quasicrystals. *Phys. Rev. B* **104** 144511 (2021).
- [36] C.-B. Hua, Zh.-R. Liu, T. Peng, R. Chen, D.-H. Xu, and B. Zhou, Disorder-induced chiral and helical Majorana edge modes in a two-dimensional Ammann-Beenker quasicrystal. *Phys. Rev. B* **104** 155304 (2021).
- [37] T. Peng, C.-B. Hua, R. Chen, Zh.-R. Liu, D.-H. Xu, and B. Zhou, Higher-order topological Anderson insulators in quasicrystals. *Phys. Rev. B* **104** 245302 (2021).
- [38] J. Jeon and S. Lee, Pattern-dependent proximity effect and Majorana edge mode in one-dimensional quasicrystals. *Phys. Rev. B* **105** 064502 (2022).
- [39] J. Fan and H. Huang, Topological states in quasicrystals. *Front. Phys.* **17** 13203 (2022).
- [40] C. Wang, F. Liu and H. Huang, Effective Model for Fractional Topological Corner Modes in Quasicrystals. *Phys. Rev. Lett.* **129**. 056403 (2022).
- [41] R. Bhola, S. Biswas, M. M. Islam, and K. Damle, Dulmage-Mendelsohn Percolation: Geometry of Maximally Packed Dimer Models and Topologically Protected Zero Modes on Site-Diluted Bipartite Lattices. *Phys. Rev. X* **12** 021058 (2022).
- [42] R. Ghadimi, M. Hori, T. Sugimoto, and T. Tohyama, Confined states and topological phases in two-dimensional quasicrystalline π -flux model. *Phys. Rev. B* **108** 125104 (2023).
- [43] R. Chen, B. Zhou, and D.-H. Xu, Quasicrystalline second-order topological semimetals. *Phys. Rev. B* **108** 195306 (2023).
- [44] Y.-B. Yang, J.-H. Wang, K. Li, Y. Xu, Higher-order topological phases in crystalline and non-crystalline systems: a review. *arXiv:2309.03688(2023)*.
- [45] K. Kamiya, T. Takeuchi, N. Kabeya, N. Wada, T. Ishimasa, A. Ochiai, K. Deguchi, K. Imura, and N. K. Sato, Discovery of superconductivity in quasicrystal, *Nat. Commun.* **9**, 154 (2018).
- [46] S. Sakai, N. Takemori, A. Koga, and R. Arita, Superconductivity on a quasiperiodic lattice: Extended-to localized crossover of Cooper pairs, *Phys. Rev. B* **95**, 024509 (2017).
- [47] J. Hou, H. Hu, K. Sun, and C. Zhang, Superfluid-Quasicrystal in a Bose-Einstein Condensate, *Phys. Rev. Lett.* **120**, 060407 (2018).
- [48] S. Autti, V. B. Eltsov, and G. E. Volovik, Observation of a Time Quasicrystal and Its Transition to a Superfluid Time Crystal, *Phys. Rev. Lett.* **120**, 215301 (2018).
- [49] R. N. Araujo and E. C. Andrade, Conventional superconductivity in quasicrystals, *Phys. Rev. B* **100**, 014510 (2019).
- [50] S. Sakai and R. Arita, Exotic pairing state in quasicrystalline superconductors under a magnetic field, *Phys. Rev. Research* **1**, 022002(R) (2019).
- [51] N. Takemori, R. Arita, and S. Sakai, Physical properties of weak-coupling quasiperiodic superconductors. *Phys. Rev. B* **102**, 115108 (2020).
- [52] Y. Nagai, N-independent localized Krylov Bogoliubov-de-Gennes method: Ultra-fast numerical approach to large scale inhomogeneous superconductors, *J. Phys. Soc. Jpn.* **89**, 074703 (2020).
- [53] G. Rai, S. Haas, and A. Jagannathan, Superconducting proximity effect and order parameter fluctuations in disordered and quasiperiodic systems. *Phys. Rev. B* **102** 134211 (2020).
- [54] T. Shiino, G. H. Gebresenbut, F. Denoel, R. Mathieu, U. Haussermann, and A. Rydh, Superconductivity at 1 K in Y-Au-Si quasicrystal approximants. *Phys. Rev. B* **103** 054510 (2021).
- [55] M. Khosravian and J. L. Lado, Quasiperiodic criticality and spin-triplet superconductivity in superconductor-antiferromagnet moire patterns. *Phys. Rev. Research* **3** 013262 (2021).
- [56] Y.-B. Liu, J.-J. Hao, Y. Y. Zhang, Y. Cao, W.-Q. Chen, and F. Yang, Cooper instability and superconductivity of the Penrose lattice. *Sci. China Phys. Mech. Astron.* **65** 287411 (2022).
- [57] T. Fukushima, N. Takemori, S. Sakai, M. Ichioka, and A. Jagannathan, Supercurrent Distribution on Ammann-Beenker Structure. *J. Phys.: Conf. Ser.* **2461** 012014 (2023).
- [58] T. Fukushima, N. Takemori, S. Sakai, M. Ichioka, and A. Jagannathan, Supercurrent distribution in real-space and anomalous paramagnetic response in a superconducting quasicrystal. *Phys. Rev. Research* **5** 043164 (2023).
- [59] Y.-B. Liu, Z.-Y. Shao, Y. Cao, and F. Yang, Unconventional superfluidity of superconductivity on Penrose lattice. *Sci. China Phys. Mech. Astron.* **66** 290312 (2023).
- [60] Y. Cao, Y. Zhang, Y.-B. Liu, C.-C. Liu, W.-Q. Chen, and F. Yang, Kohn-Luttinger Mechanism Driven Exotic Topological Superconductivity on the Penrose Lattice. *Phys. Rev. Lett.* **125**, 017002 (2020).
- [61] M. Cheng, K. Sun, Victor Galitski, and S. Das Sarma, Stable topological superconductivity in a family of two-dimensional fermion models. *Phys. Rev. B* **81**, 024504 (2010).
- [62] P. W. Anderson, Theory of dirty superconductors, *J. Phys. Chem. Solids* **11**, 26 (1959).
- [63] D. F. Agterberg, and H. Tsunetsugu, Dislocations and vortices in pair-density-wave superconductors. *Nat. Phys.* **4**, 639 (2008).
- [64] E. Berg, E. Fradkin, and S. A. Kivelson, Charge-4e superconductivity from pair-density-wave order in certain high-temperature superconductors. *Nat. Phys.* **5**, 830 (2009).
- [65] D. F. Agterberg, M. Geracie, and H. Tsunetsugu, Conventional and charge-six superfluids from melting hexagonal Fulde-Ferrell-Larkin-Ovchinnikov phases in two dimensions. *Phys. Rev. B* **84**, 014513 (2011).
- [66] E. Babaev, Phase diagram of planar $U(1) \times U(1)$ superconductor condensation of vortices with fractional flux and a superfluid state. *Nucl. Phys. B* **686**, 397 (2004).
- [67] W. H. Ko, P. A. Lee, and X. G. Wen, Doped kagome system as exotic superconductor. *Phys. Rev. B* **79**, 214502 (2009).
- [68] E. V. Herland, E. Babaev, and A. Sudbo, Phase transitions in a three dimensional $U(1) \times U(1)$ lattice London superconductor: metallic superfluid and charge-4e superconducting states. *Phys. Rev. B* **82**, 134511 (2010).
- [69] F. -F. Song, and G. -M. Zhang, Phase coherence of pairs of cooper pairs as quasi-long-range order of half-vortex pairs in a two-dimensional bilayer system. *Phys. Rev. Lett.* **128**, 195301 (2022).
- [70] P. Li, K. Jiang, and J. Hu, Charge 4e superconductor: a wavefunction approach. Preprint at arXiv <https://doi.org/10.48550/arXiv.2209.13905>.
- [71] L.-F. Zhang, Z. Wang, X. Hu, Higgs-Leggett mechanism for the elusive 6e superconductivity observed in Kagome vanadium-based superconductors. *arXiv:2205.08732*
- [72] S. Zhou, and Z. Wang, Chern Fermi pocket, topological pair density wave, and charge-4e and charge-6e supercon-

- ductivity in kagome superconductors. *Nat. Commun.* **13**, 7288 (2022).
- [73] Y. Yu, Nondegenerate surface pair density wave in the kagome superconductor CsV3Sb5: application to vestigial orders. *Phys. Rev. B* **108**, 054517 (2023).
- [74] M. Zeng, L. -H. Hu, H. -Y. Hu, Y. -Z. You, and C. Wu, High-order time reversal symmetry breaking normal state. *Sci. China-Phys. Mech. Astron.* (to be published). <https://www.sciengine.com/SCPMA/doi/10.1007/s11433-023-2287-8>.
- [75] M. Hecker, R. Willa, J. Schmalian, and R. M. Fernandes, Cascade of vestigial orders in two-component superconductors: Nematic, ferromagnetic, s-wave charge-4e, and d-wave charge-4e states. *Phys. Rev. B* **107**, 224503 (2023).
- [76] M. Hecker and R. M. Fernandes, Local condensation of charge-4e superconductivity at a nematic domain wall. arXiv:2311.02005
- [77] S.-K. Jian, Y. Huang, and H. Yao, Charge-4e Superconductivity from Nematic Superconductors in Two and Three Dimensions. *Phys. Rev. Lett.* **127**, 227001 (2021).
- [78] R. M. Fernandes, and L. Fu, Charge-4e Superconductivity from Multicomponent Nematic Pairing: Application to Twisted Bilayer Graphene. *Phys. Rev. Lett.* **127**, 047001 (2021).
- [79] J. Li, et al. Nematic superconducting state in iron pnictide superconductors. *Nat. Commun.* **8**, 1880 (2017).
- [80] S. Yonezawa, K. Tajiri, S. Nakata, Y. Nagai, Zh. Wang, K. Segawa, Y. Ando, and Y. Maeno, Thermodynamic evidence for nematic superconductivity in $\text{Cu}_x\text{Bi}_2\text{Se}_3$. *Nat. Phys.* **13**, 123-126 (2017).
- [81] R. Tao, Y. -J. Yan, X. Liu, Z. -W. Wang, Y. Ando, Q. -H. Wang, T. Zhang, D. -L. Feng, Direct Visualization of the Nematic Superconductivity in $\text{Cu}_x\text{Bi}_2\text{Se}_3$. *Phys. Rev. X* **8**, 041024 (2018).
- [82] I. Kostylev, S. Yonezawa, Z. Wang, Y. Ando, and Y. Maeno, Uniaxial-strain control of nematic superconductivity in $\text{Sr}_x\text{Bi}_2\text{Se}_3$. *Nat. Commun.* **11**, 4152 (2020).
- [83] D. V. Chichinadze, L. Classen, and A. V. Chubukov, Nematic superconductivity in twisted bilayer graphene. *Phys. Rev. B* **101**, 224513 (2020).
- [84] T. Le, et al. Evidence for nematic superconductivity of topological surface states in PbTaSe_2 . *Science Bulletin* **65**, 1349 (2020).
- [85] H. Tsunetsugu, T. Fujiwara, K. Ueda, and T. Tokihiro, Eigenstates in 2-Dimensional Penrose Tiling. *J. Phys. Soc. Jpn.* **55**, pp. 1420-1423 (1986).
- [86] H. Tsunetsugu, T. Fujiwara, K. Ueda, and T. Tokihiro, Electronic properties of the Penrose lattice. I. Energy spectrum and wave functions. *Phys. Rev. B* **43**, 8879 (1991).
- [87] W. Kohn and J. M. Luttinger, New Mechanism for Superconductivity, *Phys. Rev. Lett.* **15**, 524 (1965).
- [88] M. A. Baranov, A. V. Chubukov, and M. Y. Kagan, Superconductivity and superfluidity in fermi systems with repulsive interactions, *Int. J. Mod. Phys. B* **06**, 2471 (1992).
- [89] See the Supplementary Material at:....., in which we provide the datas on Anderson's theorem, ground state energy and STM, the expressions for physical quantities, the technique details and more results of the RG and MC studies.
- [90] K. Jiang and P. Zhang, Numerical methods for quasicrystals. *J. Comput. Phys.* **256**, 428 (2014).
- [91] Y. -B. Liu, J. Zhou, C. Wu, and F. Yang, Charge-4e superconductivity and chiral metal in 45° -twisted bilayer cuprates and related bilayers. *Nat. Commun.* **14**, 7926 (2023).
- [92] J. V. Jose, L. P. Kadanoff, S. Kirkpatrick, and D. R. Nelson, Renormalization, vortices, and symmetry-breaking perturbations in the two-dimensional planar model. *Phys. Rev. B* **16**, 1217 (1977).
- [93] J. Tobochnik, Properties of the q-state clock model for $q=4,5$, and 6. *Phys. Rev. B* **26**, 6201 (1982).
- [94] M. S. S. Challa and D. P. Landau, Critical behavior of the six-state clock model in two dimensions. *Phys. Rev. B* **33**, 437 (1986).
- [95] T. Surungan, S. Masuda, Y. Komura and Y. Okabe, Berezinskii-Kosterlitz-Thouless transition on regular and Villain types of q-state clock models. *J. Phys. A: Math. Theor.* **52**, 275002 (2019).
- [96] Zi-Qian Li, Li-Ping Yang, Z. Y. Xie, H.-H. Tu, H.-J. Liao, and T. Xiang, Critical properties of the two-dimensional q-state clock model. *Phys. Rev. E* **101**, 060105 (R) (2020).
- [97] H. Chen, P. Hou, S. Fang, and Y. Deng, Monte Carlo study of duality and the Berezinskii-Kosterlitz-Thouless phase transitions of the two-dimensional q-state clock model in flow representations. *Phys. Rev. E* **106**, 024106 (2022)
- [98] Y. Miyajima, Y. Murata, Y. Tanaka and M. Mochizuki, Machine learning detection of Berezinskii-Kosterlitz-Thouless transitions in q-state clock models. *Phys. Rev. B* **104**, 075114 (2021).
- [99] V. Gali, M. Hecker, and R. M. Fernandes, A critical nematic phase with pseudogap-like behavior in twisted bilayers, arXiv:2401.01844.

Appendix A: Microscopic Calculations Based on Kohn-Luttinger Mechanism

The microscopic calculations start from the standard repulsive Hubbard model on the Penrose lattice. The Cooper pairing can be driven by the Kohn-Luttinger (K-L) mechanism [1, 2], generalized to the cases on the QC [3]. In the K-L mechanism, two electrons near the Fermi level can gain effective attraction through exchanging particle-hole excitations in several second-order perturbative processes, leading to the following effective Hamiltonian:

$$H_{eff} = - \sum_{\langle i,j \rangle \sigma} t c_{i\sigma}^\dagger c_{j\sigma} + U \sum_i n_{i\uparrow} n_{i\downarrow} - \mu \sum_{i,\sigma} n_{i\sigma} - (U^2/2) \sum_{ij\sigma\sigma'} \chi_{ij} c_{i\sigma}^\dagger c_{i\sigma'} c_{j\sigma'}^\dagger c_{j\sigma}, \quad (\text{A1})$$

where $c_{i\sigma}$ annihilates an electron at site i with spin σ , $n_{i\sigma}$ is the electron-number operator, and μ denotes the chemical potential. χ_{ij} is the static susceptibility, defined as

$$\chi_{ij} = \sum_{mn} \xi_{i,m} \xi_{j,m} \xi_{i,n} \xi_{j,n} \frac{n_F(\tilde{\epsilon}_m) - n_F(\tilde{\epsilon}_n)}{\tilde{\epsilon}_n - \tilde{\epsilon}_m} \quad (\text{A2})$$

Here m labels a single-particle eigen state with eigen-energy $\tilde{\epsilon}_m = \epsilon_m - \mu$ and $\xi_{i,m}$ represents for the wave function of the state m . n_F is the Fermi-Dirac function. A BCS mean-field (MF) study on the effective Hamiltonian leads to the self-consistent gap equation, which reduces to the following linearized equation at T_c ,

$$\sum_{m'n'} F_{mn,m'n'}^{(s/t)} \tilde{\Delta}_{m'n'} = \tilde{\Delta}_{mn} \quad (\text{A3})$$

where m, n, m', n' are the state indices and s/t labels spin singlet/triplet state. See Ref [3] for the details of the interaction matrix $F^{(s/t)}$. We just consider the Cooper pairing Δ_{mn} taking place near the Fermi surface while the m, n -states belong to a narrow energy shell near the Fermi level. T_c is the temperature at which the largest eigenvalue of $F^{s/t}$ matrix attains one, and the pairing symmetry is determined by the corresponding eigenvector. The possible pairing symmetries can be classified according to the IRRPs of the D_5 point group, including 1D and 2D IRRPs. Note that the spin statistics and pairing symmetry are independent, i.e. each IRRP can have either spin-singlet or spin-triplet pairing. See Ref [3] for more details.

In the rest of this section, we present more calculation results. In subsection A, we present the distribution of the p_y -wave and s -wave gap functions near the Fermi level in the state space. In subsection B, we present the results of some experimental quantities of the gapless SC obtained in our work, including the STM spectrum, the specific heat, the NMR Knight-shift and the superfluid density. In subsection C, we present the results of the case in which the gapless chiral SC as the ground state while filling that the ground state for another filling $\delta = 0.51$.

1. Typical Gap Functions

In Fig. 4, as a supplement to the Fig.1(b) in the main text, we show distribution of the amplitude $|\Delta_{mn}|$ ($\Delta_{mn} \in \mathbb{R}$) of a typical singlet p_y - and s -wave pairing gap functions between the states m and n (labeled by their energies) near the Fermi level, with the filling $\delta = 0.49$. For each m , there is no unique n which makes $|\Delta_{mn}|$ dominate that of any other n , violating Anderson's theorem.

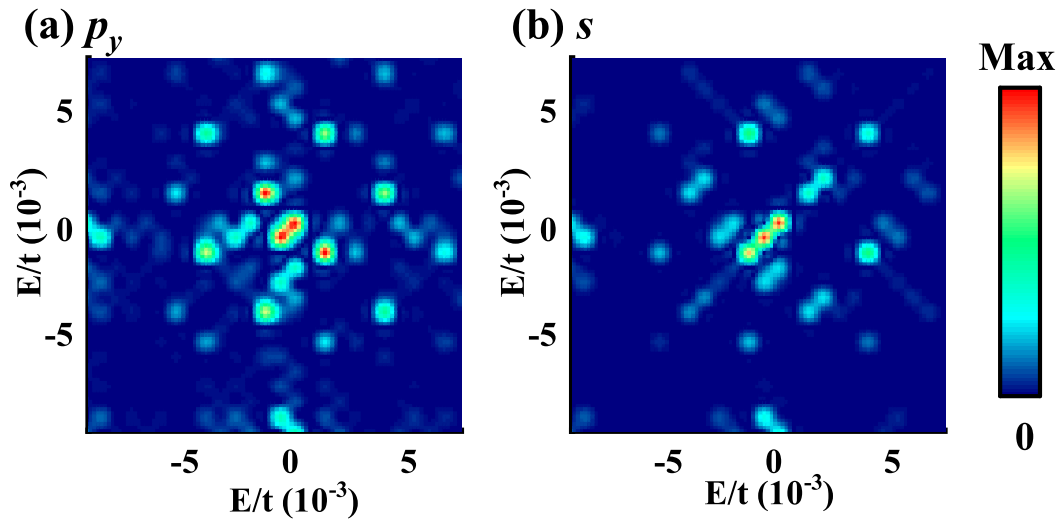


FIG. 4. (Color online) Contour plots of relative $|\Delta_{mn}|$, for a singlet p_y -wave(a) and s -wave(b) state for $\delta = 0.49$ and $U/W_D = 0.5$. The state m, n are labeled by their energies E in unit of t .

2. Experiment Quantities

In order to investigate the superconducting properties in QCs, we write out the B-dG (Bogoliubov-de Gennes) Hamiltonian matrix in the state space,

$$\begin{aligned}
 H_{\text{BCS-MF}} &= \sum_{m=1,\sigma}^{N_c} \tilde{\varepsilon}_m c_{m\sigma}^\dagger c_{m\sigma} + \sum_{mn=1}^{N_c} \left(c_{m\uparrow}^\dagger c_{n\downarrow}^\dagger - c_{m\downarrow}^\dagger c_{n\uparrow}^\dagger \right) \Delta_{mn} + h.c. \\
 &= \begin{pmatrix} \dots & & & & \\ \dots & c_{m\uparrow}^\dagger & \dots & c_{m\downarrow} & \dots \\ \dots & & & & \\ \dots & & & & \\ \dots & & & & \end{pmatrix} \begin{pmatrix} \tilde{\varepsilon} & \Delta \\ \Delta^\dagger & -\tilde{\varepsilon} \end{pmatrix} \begin{pmatrix} \dots \\ \hat{c}_{n\uparrow} \\ \dots \\ \hat{c}_{n\downarrow}^\dagger \\ \dots \end{pmatrix} \\
 &= X^\dagger H_{\text{BdG}} X = \sum_{l=1}^{2N_c} E_l \gamma_l^\dagger \gamma_l.
 \end{aligned} \tag{A4}$$

where m, n -states belong to a narrow energy shell near the Fermi level. Here the thickness of the energy shell is $0.06t$ and it includes $N_c (= 100)$ states. In subsequent text, m, n just represents states in the energy shell. The Bogoliubov transformation is written as $X = \Omega \gamma$. The amplitude of SC order parameter $|\Delta_{mn}|$ can be determined by the free energy minimization approach at finite temperatures. The expression of the free energy is

$$F = E - TS. \tag{A5}$$

where the ground energy E is the expectation value of the effective Hamiltonian, and the entropy $S = K_B \sum_l \ln(1 + e^{-\beta E_l}) + \beta E_l n_f(E_s)$, where $\beta = 1/K_B T$.

Fig.1(c) in the main text shows the SC ground state energy as a function of $|\Delta|$. It indicates that the ground state is the nematic SC when $\delta = 0.49$ and $U/W_D = 0.5$. After determining the global amplitude $|\Delta|$ of the SC order parameter by the free energy minimization approach, we investigate some experimental quantities of the nematic SC state for $\delta = 0.49$ and $U/W_D = 0.5$, including the following

- 1) The scanning tunneling microscopy (STM) dI/dV spectrum at site j can be written as

$$D(\omega) = \int \sum_{\sigma} \langle T_{\tau} c_{j\sigma}^\dagger(\tau) c_{j\sigma}(0) \rangle e^{i\omega\tau} d\tau \tag{A6}$$

The STM dI/dV spectrum are site dependent, distinct from the periodic lattice. The STM dI/dV curve for a typical site is shown in the Fig. 1(d) in the main text. For generality, Fig. 5 shows the STM dI/dV curve on additional typical sites for both nematic SC (blue line), chiral SC (red line) and normal state (black line), and all STM dI/dV curve in the main text and Fig. 5 indicates that both the nematic and chiral SC states in this model can be gapless.

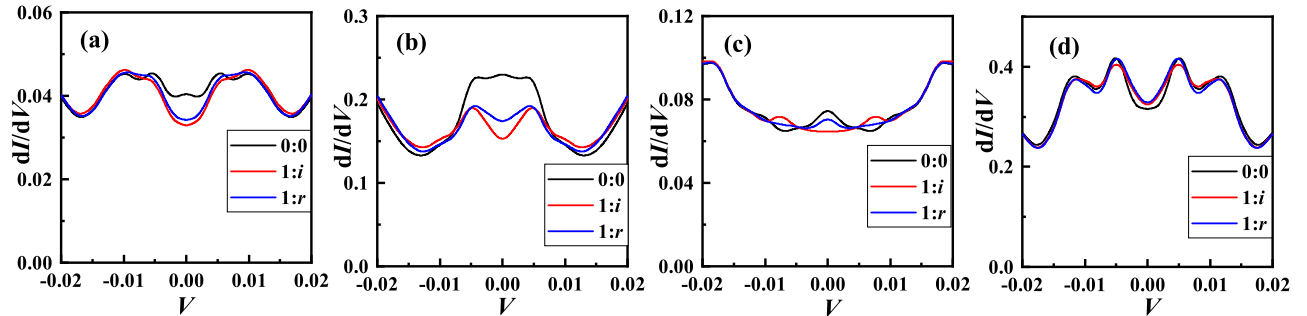


FIG. 5. (Color online) The STM dI/dV spectra of some typical sites for the nematic SC (blue line), the chiral SC (red line) and the normal state (black line). V is in unit of t .

2) The specific heat C_v is given by

$$C_v = T \frac{\partial S}{\partial T} \quad (\text{A7})$$

Fig. 6(a) shows the specific heat for the nematic SC as a function of temperature T . In the low- T region, except for a tiny finite-size gap, the specific heat is proportional to temperature, similar to the behavior in Fermi liquid (FL).

3) The Knight-shift is given by

$$K = \int \langle T_\tau S^+(\tau) S^-(0) \rangle e^{i\omega\tau} d\tau \quad (\text{A8})$$

where $S^+ = \sum_i c_{i\uparrow}^\dagger c_{i\downarrow}$ and $S^- = \sum_i c_{i\downarrow}^\dagger c_{i\uparrow}$. Fig. 6(b) exhibits that the NMR Knight-shift K for nematic SC saturates to a finite value in the low temperature region, similarly to the Pauli-susceptibility behavior for standard FL.

4) The superfluid density ρ is related to the current J given by

$$J_\alpha(\mathbf{A}) = - \sum_{\langle ij \rangle > \sigma} \frac{1}{2} t_{ij} R_{ij,\alpha} (i - \mathbf{R}_{ij,\alpha} \mathbf{A}) \langle c_{i\sigma}^\dagger c_{j\sigma} \rangle + c.c. \quad (\text{A9})$$

where \mathbf{A} is the magnetic vector potential and $\alpha = (x, y)$ is the direction of the current. The superfluid density $\rho = \mathbf{J}/\mathbf{A}$ at the limit $\mathbf{A} \rightarrow 0$. Fig. 6(c) shows the current as a function of the magnetic vector potential \mathbf{A} at different temperatures. The finite \mathbf{J}/\mathbf{A} ratio is consistent with the Meissner effect, confirming the SC state. Fig. 6(d) shows the finite superfluid density $\rho > 0$ in the low-temperature region, and $\rho = 0$ when $T > T_c$.

In a summary, according to the above experimental quantities, it is evident that the ground state is the gapless nematic SC for $\delta = 0.49$ and $U/W_D = 0.5$.

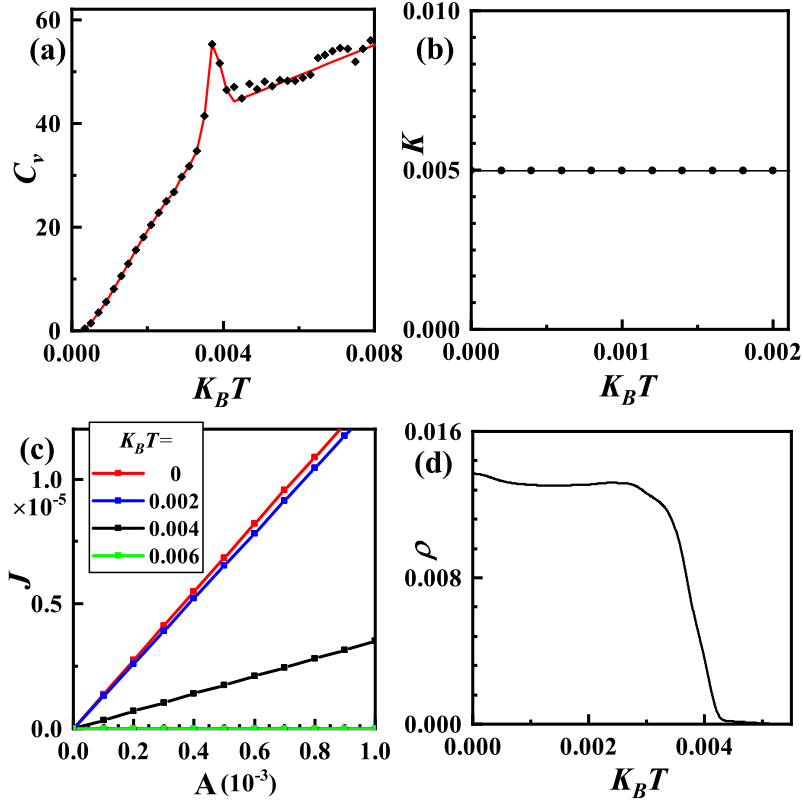


FIG. 6. (Color online) Experiment-relevant quantities for the gapless nematic SC obtained by our calculations. The temperature $K_B T$ is in units of t . (a) The specific heat C_v as function of T . (b) The NMR Knight-shift K as function of T . (c) The current J as function of the exerted vector potential \mathbf{A} at several temperatures. (d) The superfluid density ρ as function of T .

3. The ground state for $\delta = 0.51$ and $U/W_D = 0.35$

We have confirmed that the ground state is the nematic SC for $\delta = 0.49$. For comparison, we have also calculated the ground state properties for another typical filling $\delta = 0.51$ and band width $W_D = 0.35$. In Fig. 7(a), we show distribution of the amplitude $|\Delta_{mn}|$ ($\Delta_{mn} \in \mathbb{R}$) of a typical singlet d_{xy} -wave pairing gap function between the states m and n (labeled by their energies) near the Fermi level, obtained at the filling $\delta = 0.51$. Fig. 7(a) indicates that for each m , there is no unique n rendering $|\Delta_{mn}|$ dominates that of any other n , violating Anderson's theorem. To determine the realized ground state, we calculate the ground state energy E as a function of the global amplitude Δ for the $1:r$ (minimized for r) and $1:i$ mixing cases. As shown in Fig. 7(b), the energy of the $1:i$ mixing is lower, indicating that the ground state is the chiral SC. Fig. 7(c) shows the local DOS detected by the STM dI/dV curve for a typical site, indicating that both the chiral SC and the nematic SC are gapless.

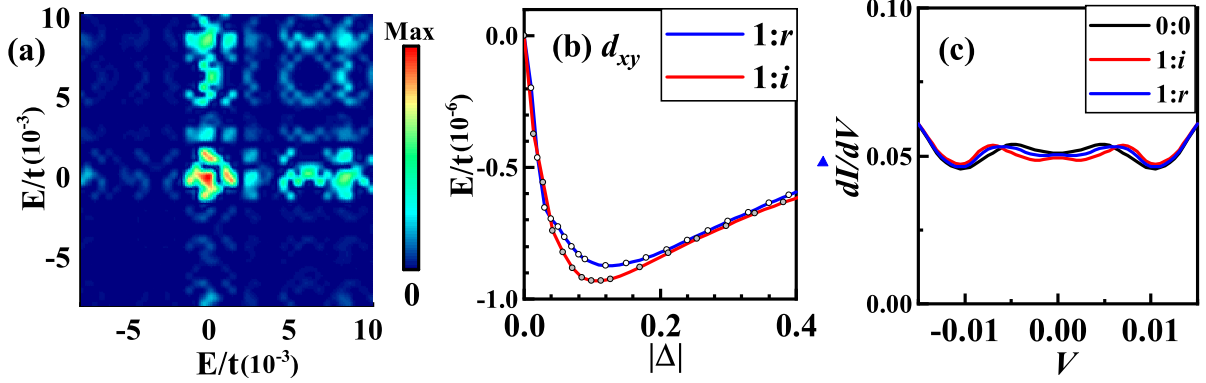


FIG. 7. (Color online) Some quantities for $\delta = 0.51$ and $U/W_D = 0.35$. The energy E and V are in unit of t . (a) Contour plots of relative $|\Delta_{mn}|$, for a singlet d_{xy} -wave state. (b) The SC ground state energy E is a function of the global magnitude $|\Delta|$ of the order parameter, and the mixture of the two degenerate form factors is $1:r$ (blue line) and $1:i$ (red line), where r is a real number. (c) The STM of a typical site for the nematic SC (blue line), chiral SC (red line) and normal state (black line).

Appendix B: G-L Theoretical analysis

The pairing symmetries on the Penrose lattice have been classified according to the irreducible representations (IRRs) of the D_5 point group [3], which includes the 1D A_1 (s-wave), A_2 (h-wave) and 2D E_1 ((p_x, p_y) -wave), E_2 ($(d_{x^2-y^2}, d_{xy})$ -wave) pairings. Here we consider the 2D E_1 IRRP, which corresponds to the (p_x, p_y) -wave pairing. The two basis functions of this pairing are denoted as $(\Delta_{p_x}, \Delta_{p_y})$. For convenience, we rotate the bases and define $\Delta_{\pm} = \Delta_{p_x} \pm i\Delta_{p_y}$. The general pairing gap function for the p -wave is a mixing of Δ_+ and Δ_- , and should take the form of

$$\Delta = \psi_+ \Delta_+ + \psi_- \Delta_- \quad (\text{B1})$$

Fixing the form factor Δ_{\pm} , the free energy F is functional of the global amplitude ψ_{\pm} .

The G-L free energy functional $F(\psi_+, \psi_-)$ should be invariant under the rotation C_5^1 , the U(1) gauge and the mirror-reflection σ operations. Under these symmetry operations, the arguments ψ_{\pm} are transformed as

$$\begin{aligned} (1) \text{ U(1)-gauge : } & \psi_{\pm} \rightarrow e^{i\theta} \psi_{\pm} \\ (2) \text{ C}_5^1\text{-rotation : } & \psi_{\pm} \rightarrow e^{\pm i2\pi/5} \psi_{\pm} \\ (3) \text{ } \sigma\text{-mirror : } & \psi_{\pm} \rightarrow \psi_{\mp} \end{aligned} \quad (\text{B2})$$

The functional $F(\psi_+, \psi_-)$ should be invariant under the above transformations (B2) on its argument.

Up to $O(\psi_{\pm}^4)$, the form of F allowed by the above symmetries takes the following form,

$$\begin{aligned} F &= F^{(2)} + F^{(4)} \\ F^{(2)} &= \alpha(|\psi_+|^2 + |\psi_-|^2) \\ F^{(4)} &= \beta(|\psi_+|^4 + |\psi_-|^4) + \gamma|\psi_+|^2|\psi_-|^2 \end{aligned} \quad (\text{B3})$$

Consequently, we have

$$\begin{aligned} F &= \alpha(|\psi_+|^2 + |\psi_-|^2) + \beta(|\psi_+|^4 + |\psi_-|^4) + \gamma|\psi_+|^2|\psi_-|^2 + o(\psi^6) \\ &= \beta(|\psi_+|^2 + |\psi_-|^2 + \alpha/2\beta)^2 + (\gamma - 2\beta)|\psi_+|^2|\psi_-|^2 + O(\psi^6) \end{aligned} \quad (\text{B4})$$

If $\gamma - 2\beta > 0$, we get $\psi_+ = 0$ or $\psi_- = 0$ to minimize the free energy. In this case, the ground state is the chiral SC, such as $p \pm ip$ -wave SC. In the contrary, $|\psi_+|/|\psi_-| = 1$ while $\gamma - 2\beta < 0$, and the ground state is the nematic SC.

To study the effects of the thermal fluctuations around the nematic-SC saddle point, we set $\psi_+ = e^{i(\theta+\phi)}\psi_0$ and $\psi_- = e^{i(\theta-\phi)}\psi_0$. Here we focus on the low-energy phase fluctuations, and have set the global amplitude $\psi_0 > 0$ as a constant. The phase fields θ and ϕ are smooth functions of the coarse-grained position \mathbf{r} . In order to derive the free energy as an explicit function of θ and ϕ , we need to expand the free energy to higher order of the ψ_{\pm} field.

Up to $O(\psi_{\pm}^6)$, the invariance of $F^{(6)}$ under the U(1)-gauge and the σ -mirror transformations in (B2) dictates

$$F^{(6)} = A|\psi_0|^6 + B|\psi_0|^4\psi_+\psi_-^* + C|\psi_0|^2\psi_+^2\psi_-^{*2} + D\psi_+^3\psi_-^{*3} + c.c. \quad (\text{B5})$$

However, under the C_5^1 rotation transformation, it is transformed as

$$F^{(6)} \rightarrow A|\psi_0|^6 + Be^{4\pi i/5}|\psi_0|^4\psi_+\psi_-^* + Ce^{8\pi i/5}|\psi_0|^2\psi_+^2\psi_-^{*2} + De^{12\pi i/5}\psi_+^3\psi_-^{*3} + c.c. \quad (\text{B6})$$

The invariance of $F^{(6)}$ under this transformation dictates $B = C = D = 0$. Consequently, $F^{(6)}$ is still not explicit functional of the θ and ϕ fields. The case for $F^{(8)}$ is similar. However, the situation is distinct for $F^{(10)}$, as it can take the following form allowed by the symmetries,

$$\begin{aligned} F^{(10)} &= -A_0(\psi_+^5\psi_-^{*5} + \psi_-^5\psi_+^{*5}) \\ &= -A \cos(10\phi) \end{aligned} \quad (\text{B7})$$

where $A = 2A_0\psi_0^{10}$. Obviously, $F^{(10)}$ is invariant under all symmetry transformation operations in Eq.(B2), and it contributes to the anisotropic part of Hamiltonian in Eq.(5) in the main text.

We can generalize the above derivation to general cases. For the nematic SC on a D_{2n} -symmetric lattice ($n \in \mathbf{Z}$), such as on the honeycomb lattice ($n = 3$), in order to derive the free energy as an explicit function of the θ and ϕ fields, we need to expand the free energy up to $2n$ -th order of its argument ψ_{\pm} . The symmetry-allowed $2n$ -th order term in the free energy is

$$F^{(2n)} = -A_0(\psi_+^n\psi_-^{*n} + \psi_-^n\psi_+^{*n}) \quad (\text{B8})$$

This term contributes to the anisotropy-field part $F^{(2n)} = -2A_0\psi_0^{2n} \cos(2n\phi)$ in the low-energy classical Hamiltonian. For the nematic SC on a D_{2n+1} symmetric lattice ($n \in \mathbf{Z}$), such as the Penrose lattice ($n = 2$). In order to derive the free energy as an explicit function of θ and ϕ , we need to expand the free energy up to $2(2n+1)$ -th order of its arguments ψ_{\pm} , leading to

$$F^{(2(2n+1))} = -A_0(\psi_+^{2n+1}\psi_-^{*2n+1} + \psi_-^{*2n+1}\psi_+^{2n+1}) \quad (\text{B9})$$

This term contributes to the anisotropy-field part $F^{(2(2n+1))} = -2A_0\psi_0^{2n} \cos[2(2n+1)\phi]$ in the low-energy effective Hamiltonian.

Appendix C: The RG Analysis and More Details

By the standard RG analysis, the flow equations at the one-loop level are given by:

$$\begin{aligned} \frac{dg_{2,0}}{d \ln b} &= (2 - \pi\rho')g_{2,0} \\ \frac{dg_{0,2}}{d \ln b} &= (2 - \pi\kappa')g_{0,2} \\ \frac{dg_{1,1}}{d \ln b} &= \left(2 - \frac{\pi}{4}(\rho' + \kappa')\right)g_{1,1} \\ \frac{dg_{10}}{d \ln b} &= \left(2 - \frac{25}{\pi\kappa'}\right)g_{10} \\ \frac{d\rho'}{d \ln b} &= -16g_{2,0}^2\rho'^3 - \frac{g_{1,1}^2}{2}\rho'^2(\rho' + \kappa') \\ \frac{d\kappa'}{d \ln b} &= \frac{10000g_{10}^2}{\pi^4\kappa'} - 16g_{0,2}^2\kappa'^3 - \frac{g_{1,1}^2}{2}\kappa'^2(\rho' + \kappa'). \end{aligned} \quad (\text{C1})$$

Here b is the renormalization scale, $g_{2,0}$, $g_{0,2}$ and $g_{1,1}$ represent the fugacities of the θ -vortices, ϕ -vortices, and half θ -half ϕ vortices. $\rho' = \rho/T$ and $\kappa' = \kappa/T$ represent two kinds of stiffness parameters.

TABLE II. Fixed points of the coupling parameters under RG, and the corresponding phases. The abbreviations denote: 4e-SC is charge-4e SC; Q-N SC is quasi-nematic SC; Q-N MT is quasi-nematic metal; N-SC is nematic SC; MT is normal metal.

$g_{2,0}$	$g_{0,2}$	g_{10}	$g_{1,1}$	ρ'	κ'	phase
∞	∞	0	∞	0	0	MT
0	∞	0	0	finite	0	4e-SC
∞	0	0	0	0	finite	Q-N MT
0	0	0	0	finite	finite	Q-N SC
0	0	∞	0	finite	∞	N-SC

In Table II, we present five fixed points of the RG flow Eq.(C1) and the corresponding phases, which appear in our numerical results.

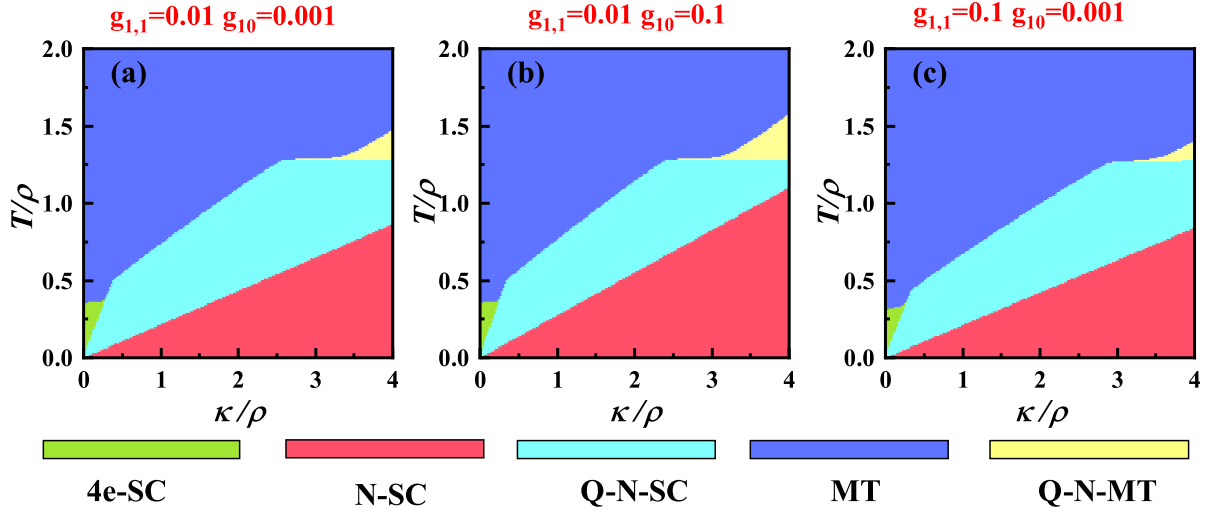


FIG. 8. (Color online) The RG phase diagrams presented with different initial coupling parameters. The coupling parameter values are set as $g_{2,0} = g_{0,2} = 0.1$, $g_{1,1} = 0.01$ and $g_{10} = 0.001$ in (a), $g_{2,0} = g_{0,2} = 0.1$, $g_{1,1} = 0.01$ and $g_{10} = 0.1$ in (b), and $g_{2,0} = g_{0,2} = 0.1$, $g_{1,1} = 0.1$ and $g_{10} = 0.001$ in (c).

We present more results provided by RG method in Fig.(8) to compare the phase diagrams with different initial values of the coupling parameters. As shown in Fig.(8), we find the regime of the nematic SC and the quasi-nematic metal phase are slightly enlarged with larger anisotropic parameter g_{10} . Furthermore, the transition line between the quasi-nematic-SC and the normal metal phase is slightly enhanced while the regime of the quasi-nematic metal phase is slightly suppressed if we increase the fugacities of the half ϕ -half θ vortices coupling parameter $g_{1,1}$. On the whole, the topology of the phase diagram is insensitive to the initial values of the coupling parameters.

Appendix D: More Details and Results About the MC Study

To perform the MC study, we discretize the Hamiltonian Eq.(5) in the main text on a square lattice as

$$\begin{aligned}
H = & -\alpha \sum_{\langle ij \rangle} \cos[\theta_+(\mathbf{r}_i) + \theta_-(\mathbf{r}_i) - \theta_+(\mathbf{r}_j) - \theta_-(\mathbf{r}_j)] \\
& - \lambda \sum_{\langle ij \rangle} \cos[\theta_+(\mathbf{r}_i) - \theta_-(\mathbf{r}_i) - \theta_+(\mathbf{r}_j) + \theta_-(\mathbf{r}_j)] \\
& - \gamma \sum_{\langle ij \rangle} \cos[\theta_+(\mathbf{r}_i) - \theta_+(\mathbf{r}_j)] + \cos[\theta_-(\mathbf{r}_i) - \theta_-(\mathbf{r}_j)] \\
& + A \sum_i \cos[2\theta_+(\mathbf{r}_i) - 2\theta_-(\mathbf{r}_i)].
\end{aligned} \tag{D1}$$

Here $\langle ij \rangle$ represents nearest-neighbor bonding, and the positive coefficients α , λ and γ satisfy,

$$\alpha = \frac{\rho - 2\gamma}{4}, \quad \lambda = \frac{\kappa - 2\gamma}{4}, \tag{D2}$$

which ensure that the discretized Hamiltonian (D1) is consistent with the continuous Hamiltonian in the thermodynamic limit. Note that the γ -term energetically realizes the ‘‘kinematics constraint’’ of the θ and ϕ fields on the discrete lattice, which was first proposed in Ref [4], and is explained in the following.

The $\theta(\mathbf{r})$ and $\phi(\mathbf{r})$ fields are related to the $\theta_{\pm}(\mathbf{r})$ fields via the relation $\theta_{\pm}(\mathbf{r}) = \theta(\mathbf{r}) \pm \phi(\mathbf{r})$. In the continuous space, the physical $\theta_{\pm}(\mathbf{r})$ phase fields should host only integer vortices, which dictates that the θ and ϕ fields should host integer or half-integer vortices simultaneously. This is the ‘‘kinematics constraint’’ between the θ and ϕ fields. On the discrete lattice, the $\alpha(\lambda)$ term energetically allows for integer or half-integer $\theta(\phi)$ vortices, otherwise the energy diverges as $O(L)$ which cannot be compensated by the entropy. For the same reason, the γ term only energetically allows for integer θ_+ or θ_- vortices, which dictates that the θ and ϕ fields should host integer or half-integer vortices simultaneously. Therefore, the γ -term energetically imposes the ‘‘kinematics constraint’’ between the θ and ϕ fields, which ensures the correct low-energy ‘‘classical Hilbert space’’ in the continuum limit. For thermodynamic limit, even an infinitesimal γ can energetically guarantee the ‘‘kinematic constraint’’. In the MC calculations, we set $\gamma = \frac{1}{4}\rho\kappa/(\rho + \kappa)$, $A = 0.025\rho$, and slight adjustments of the parameters will not qualitatively change the results, including the topology of the phase diagram.

We can determine the phase diagram based on the decaying behavior of the correlation functions $\eta_{\phi/\theta}$. The Table III provides the decaying behavior of the correlation functions $\eta_{\phi/\theta}$ for all possible phases. In the main text, we present the $\eta_{\phi/\theta}$ for the representative B(Q-N SC) and C(Q-N MT) points marked in the MC phase diagram, and their decaying behaviors are consistent with the Table III. As supplements, Fig. 9(a) and (b) show Δr -dependence of η_{θ} and η_{ϕ} for the representative point A marked in the MC phase diagram in the main text. Obviously, η_{ϕ} decays exponentially with Δr , η_{θ} decays in power law with Δr , consistent with the properties of the 4e-SC phase. Fig. 9(c) and (d) show the cases for the representative point D marked in the MC phase diagram in the main text: η_{θ} decays in power law with Δr , η_{ϕ} saturates to a nonzero value when $\Delta r \rightarrow \infty$, consistent with the properties of the N-SC phase. Fig. 9(e) and (f) show the cases for the representative point E marked in the MC phase diagram in the main text. Both correlation functions decay exponentially with Δr , consistent with the properties of the MT phase.

TABLE III. The decaying behavior of the correlation functions η_{ϕ} and η_{θ} for all possible phases. The abbreviations denote: 4e-SC is charge-4e SC; Q-N SC is quasi-nematic SC; Q-N MT is quasi-nematic metal; N-SC is nematic SC; MT is normal metal.

Phase	η_{ϕ}	η_{θ}
4e-SC	$e^{-r/\xi}$	$r^{-\sigma}$
Q-N SC	$r^{-\sigma_1}$	$r^{-\sigma_2}$
Q-N MT	$r^{-\sigma}$	$e^{-r/\xi}$
N-SC	const	$r^{-\sigma}$
MT	e^{-r/ξ_1}	e^{-r/ξ_2}

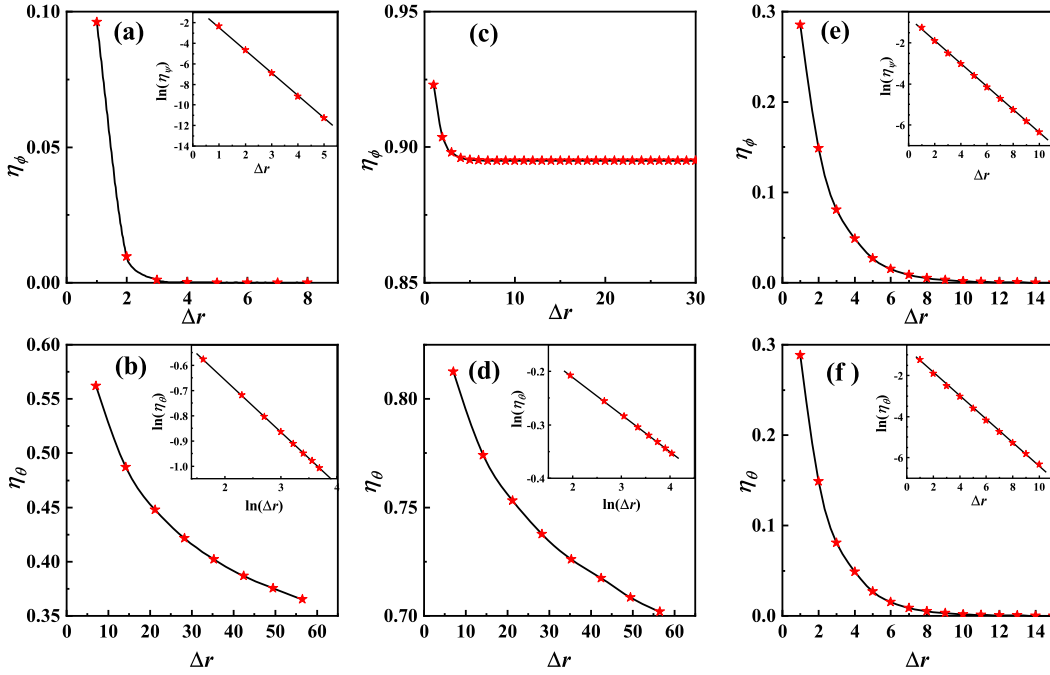


FIG. 9. (Color online) The correlation function $\eta_{\phi/\theta}$ for (a) and (b) for A($\kappa = 0.2\rho, T = 0.2\rho$), representing for the 4e-SC phase), for (c) and (d) for D($\kappa = \rho, T = 0.1\rho$), representing for the N-SC phase) and for (e) and (f) for E($\kappa = 1\rho, T = 0.35\rho$), representing for the MT phase) marked in Fig.2(b) of the main text. Insets of (b,d) the log-log plot, and (a,e-f) only the y-axes are logarithmic.

In addition to the correlation functions, some physical quantities can effectively determine the phase diagram and the phase transition temperatures T_c . To establish the phase diagram, we calculate the following physical quantities:

- 1) The specific heat is given as

$$C_v = \frac{\langle H^2 \rangle - \langle H \rangle^2}{NT^2}. \quad (\text{D3})$$

Broad bumps in the specific heat may indicate phase transitions. However, in some cases, the BKT transition is featureless in the C_v curve.

- 2) The stiffness of the θ -field can be obtained through the approach introduced in Ref.[5]. The stiffness S characterizes the superfluid density. Non-zero S indicates the presence of SC.

- 3) The susceptibility χ and Binder cumulant U of θ and ϕ are defined as [6]

$$\chi = \frac{N(\langle m^2 \rangle - \langle m \rangle^2)}{K_B T}, \quad U = 1 - \frac{\langle m^4 \rangle}{3\langle m^2 \rangle^2}, \quad (\text{D4})$$

where $m = \frac{1}{N} \sum_i e^{i\theta}$ for the θ -field or $m = \frac{1}{N} \sum_i e^{i\phi}$ for the ϕ -field, and N is the lattice-site number. Divergence of $\chi_{\theta/\phi}$ implies θ/ϕ is quasi-long-range order, while finite $\chi_{\theta/\phi}$ indicates θ/ϕ is either long-range order or disorder. The Binder cumulant $U_{\theta/\phi}$ characterizes the order degree of θ/ϕ . When the θ/ϕ -field is disordered, the quantity $3U_{\theta/\phi} - 1 = 0$; when the θ/ϕ -field is long-range ordered or quasi-long-range ordered, the quantity $3U_{\theta/\phi} - 1 = 1$.

In Fig. 10, we show the above quantities as functions of temperature for different lattice sizes at $\kappa/\rho = 0.3, 1$ and 2.2. More detailedly, Fig. 10(a1-a3) shows the specific heat C_v , Fig. 10(b1-b3) shows the stiffness S_θ , Fig. 10(c1-c3) and (e1-e3) shows the susceptibility χ_θ and χ_ϕ , and Fig. 10(d1-d3) and (f1-f3) shows the Binder cumulant $3U_\theta - 1$ and $3U_\phi - 1$, respectively.

For $\kappa/\rho = 0.3$, the results are shown in Fig. 10(a1,b1,...,f1). When the temperature T/ρ rises to about 0.05, the specific heat exhibits a finite broad bump, and the susceptibility χ_ϕ changes from finite to divergence, which suggests that the ϕ -field experiences a BKT phase transition from long-range order to quasi-long-range order at $T/\rho \approx 0.05$. The system enters the Q-N SC phase upon this BKT transition. Next, when T/ρ rises to about 0.15, the specific heat exhibits a finite broad bump, the susceptibility χ_ϕ transitions from divergence to finite, and the cumulant $3U_\phi - 1$

rapidly drops to zero, which suggesting that ϕ -field experiences another BKT phase transition from quasi-long-range order to disorder at $T/\rho \approx 0.15$. The system enters the 4e-SC phase upon this BKT transition. Finally, when T/ρ rises to about 0.24, the specific heat exhibits a finite broad bump, the stiffness S_θ rapidly drops to zero, the susceptibility χ_θ changes from divergence to finite, and the cumulant $3U_\theta - 1$ rapidly drops to zero. These features suggest that the θ -field experiences a BKT phase transition from quasi-long-range order to disorder at $T/\rho \approx 0.24$. The system enters the normal MT phase upon this BKT transition.

For $\kappa/\rho = 1$, the results are shown in Fig. 10(a2,b2,...,f2). When the temperature T/ρ rises to about 0.143, the specific heat is very smooth, and the susceptibility χ_ϕ changes from finite to divergence, which suggests that the ϕ -field experiences a BKT phase transition from long-range order to quasi-long-range order at $T/\rho \approx 0.143$. The system enters the Q-N SC phase upon this BKT transition. Next, when T/ρ rises to about 0.32, the specific heat exhibits a finite broad bump, the stiffness S_θ rapidly drops to zero, the susceptibility χ_θ and χ_ϕ changes from divergence to finite, and the Binder cumulant $3U_\theta - 1$ and $3U_\phi - 1$ rapidly drop to zero, which suggests that the ϕ - and θ - fields simultaneously experience a BKT phase transition from quasi-long-range order to disorder at $T/\rho \approx 0.32$. The system enters the normal MT phase upon this BKT transition.

For $\kappa/\rho = 2.2$, the results are shown in Fig. 10(a3,b3,...,f3). When temperature T/ρ rises to about 0.31, the specific heat is very smooth, and the susceptibility χ_ϕ changes from finite to divergence, which suggests that the ϕ -field experiences a BKT phase transition from long-range order to quasi-long-range order at $T/\rho \approx 0.31$. The system enters the Q-N SC phase upon this BKT transition. Next, when T/ρ rises to about 0.44, the specific heat exhibits a finite broad bump, the stiffness S_θ rapidly drops to zero, the susceptibility χ_θ changes from divergence to finite, and the Binder cumulant $3U_\theta - 1$ rapidly drops to zero. These results suggest that the θ -field experiences a BKT phase transition from quasi-long-range order to disorder at $T/\rho \approx 0.44$. The system enters the Q-N MT phase upon this BKT transition. Finally, when T/ρ rises to about 0.53, the specific heat exhibits a shoulder, the susceptibility χ_ϕ changes from divergence to finite, and the Binder cumulant $3U_\phi - 1$ rapidly drops to 0, which suggests that the ϕ -field experiences a BKT phase transition from quasi-long-range order to disorder at $T/\rho \approx 0.53$. The system enters the normal MT phase upon this BKT transition.

* These two authors contributed equally to this work.

† yangfan_blg@bit.edu.cn

- [1] W. Kohn and J. M. Luttinger, Phys. Rev. Lett. **15**, 524 (1965).
- [2] M. A. Baranov, A. V. Chubukov, and M. Y. Kagan, Int. J. Mod. Phys. B **06**, 2471 (1992).
- [3] Y. Cao, Y. Zhang, Y.-B. Liu, C.-C. Liu, W.-Q. Chen, and F. Yang, Phys. Rev. Lett. **125**, 017002 (2020).
- [4] Y. -B. Liu, J. Zhou, C. Wu, and F. Yang, Nat. Commun. **14**, 7926 (2023).
- [5] M. Zeng, L.-H. Hu, H.-Y. Hu, Y.-Z. You, and C. Wu, arXiv: 2102.06158.
- [6] M. S. S. Challa, and D. P. Landau, Phys. Rev. B **33**, 437 (1985).

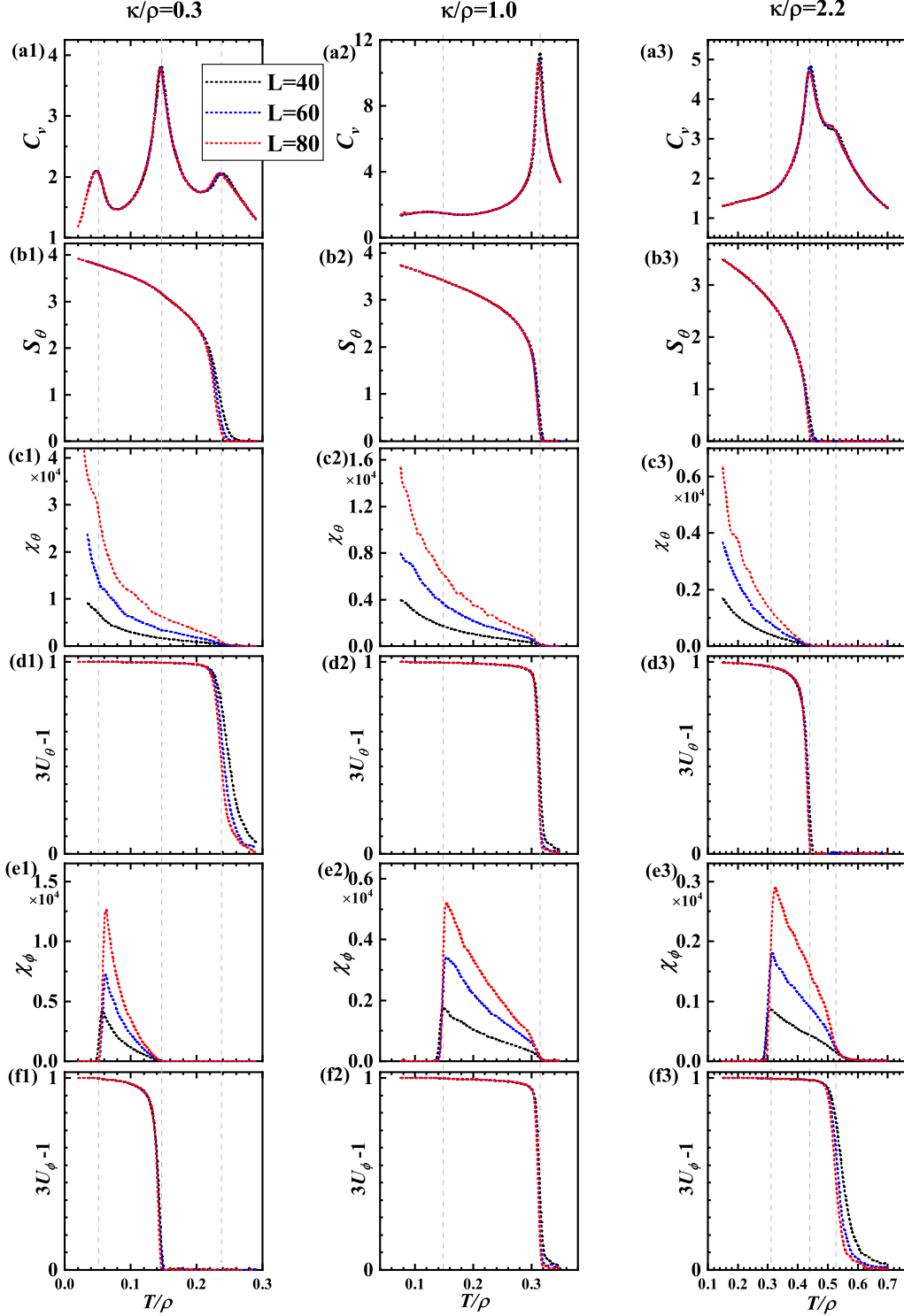


FIG. 10. (Color online) Various T -dependent quantities for $\kappa/\rho = 0.3$ (a1,b1,...,f1), $\kappa/\rho = 1$ (a2,b2,...,f2) and $\kappa/\rho = 2.2$ (a3,b3,...,f3). The scaling in all figures is $L = 40$ (black line), 60 (blue line), and 80 (red line). (a1-a3) The specific heat C_v . (b1-b3) The stiffness S_θ of θ . (c1-c3) The susceptibilities χ_θ of θ . (d1-d3) $3U_\theta - 1$, where U_θ is the Binder cumulant of the θ -field. (e1-e3) The susceptibilities χ_ϕ of ϕ . (f1-f3) $3U_\phi - 1$, where U_ϕ is the Binder cumulant of the ϕ -field.